Book of Tutorials and Abstracts

European Microbeam Analysis Society

EMAS 2023

17th

EUROPEAN WORKSHOP

on

MODERN DEVELOPMENTS AND APPLICATIONS IN MICROBEAM ANALYSIS

7 to 11 May 2023
at the
Jagiellonian University, Auditorium Maximum
Krakow, Poland

Under the auspices of the Rector of the
Jagiellonian University, Krakow, Poland
Organised in collaboration with the
Institute of Metallurgy and Materials Science of
the Polish Academy of Sciences, Krakow, Poland

EMAS
European Microbeam Analysis Society eV
www.microbeamanalysis.eu/

This volume is published by:
European Microbeam Analysis Society eV (EMAS)
EMAS Secretariat
c/o Eidgenössische Technische Hochschule, Institut für Geochemie und Petrologie
Clausiusstrasse 25
8092 Zürich
Switzerland

© 2023 *EMAS* and authors

ISBN 978 90 8227 6961
NUR code: 972 – Materials Science

All rights reserved. No part of this publication may be reproduced, stored in a retrieval system, or transmitted in any form or by any means, electronic, mechanical, by photocopying, recording or otherwise, without the prior written permission of *EMAS* and the authors of the individual contributions.

SUBSCALE INVERSION OF X-RAY EMISSION IN ELECTRON PROBE MICROANALYSIS BASED ON DETERMINISTIC TRANSPORT EQUATIONS

G. Achuda[1], T. Claus[2], S. Richter[1] and Manuel Torrilhon[2]

1 RWTH Aachen University, Central Facility for Electron Microscopy (GFE)
Ahornstrasse 55, 52074 Aachen, Germany
2 RWTH Aachen University, Applied and Computational Mathematics
Schinkelstrasse 2, 52062 Aachen, Germany
e-mail: mt@mathcces.rwth-aachen.de

Manuel Torrilhon is full professor in Applied and Computational Mathematics at RWTH Aachen University in Germany, and heads the mathematics division of the study program 'Computational Engineering Science (CES)' at RWTH. He holds a diploma degree in Engineering Physics from Technical University of Berlin, Germany, and received a PhD in Applied Mathematics from ETH Zurich, Switzerland in 2004. After postdoc years at Hong Kong University of Science and Technology and at Princeton University (USA), he joined ETH Zurich as junior faculty funded by a European Science Foundation ERC-type grant before accepting the position at RWTH Aachen in 2010. His research focus is on numerical methods for and mathematical modelling with partial differential equations, in particular hyperbolic conservation laws, kinetic theory, Boltzmann equation and plasma physics. Since 2014 he works with the Laboratory for Electron Microscopy (GFE) at RWTH Aachen on mathematical algorithms for the inverse problem of EPMA. So far, this collaboration was successful in two funding rounds of the German Research Foundation (DFG) and produced several publications.

1. INTRODUCTION

In electron probe microanalysis (EPMA) the sample is excited by a focussed beam of electrons, which generates X-rays that are characteristic to the chemical components of the sample. The measured X-ray intensity $I_{(Z,j)}$, for atomic number Z of the associated atom and a transition j is normalised into an experimental k-ratio $k^{\mathrm{exp}}_{(Z,j)} = I_{(Z,j)}/I^{\mathrm{std}}_{(Z,j)}$ by the intensity of a standard sample.

An experiment yields multiple k-ratios: one for each of the considered characteristic X-ray transitions. Additionally, the experimental setup $\boldsymbol{u}$, e.g., the beam position, energy or angle, can be varied to obtain more information about the material. To reconstruct the spatial distribution of the chemical composition of the sample, the collection of all k-ratios $k = \{k^{u_1}_{(Z,j)}, \ldots, k^{u_2}_{(Z,j)}, \ldots\}$ must be post-processed by an inversion algorithm, see also Fig. 1.

In this work, we consider mass concentrations $\rho : \mathbb{R}^3 \to \mathbb{R}^{n_e}, x \mapsto \rho(x)$ as the general description of compounds in the sample. n_e is the number of constituents. The X-ray intensity will depend on $\rho(x)$, and, hence, the general reconstruction problem is given by

$$\rho^*(x) = \arg\min_{\rho(x)} \mathrm{disc}(k(\rho(x)), k^{\mathrm{exp}}) \tag{1}$$

where $\rho^*(x)$ is the true distribution of mass concentrations. The unique reconstruction of the infinite dimensional field $\rho^*(x)$ from a finite set of measurements k^{exp} is only possible with additional constraints or prior assumptions. Additionally, the precise representation of uncertainty in $\rho^*(x)$ is a useful approach. In the mathematical framework of inverse problem theory, knowing the uncertainty of the unknown $\rho^*(x)$ is defined as the solution of the inverse reconstruction problem. Prior knowledge about the material and the additional knowledge based on the experimental measurements reduces general ignorance of $\rho^*(x)$.

2. RECONSTRUCTIONS AND REGULARISATION

The representation of the unknown $\rho(x)$ as a function has infinite dimensions. Therefore, it can not be reconstructed from a finite set of data k^{exp} even in the absence of noise. The inverse problem is considered as being ill-posed, because no unique solution exists. To mitigate the ill-posed behaviour of the inverse problem, regularisation adds information. Thus, it is closely connected to the definition of prior knowledge about the material ρ from inverse problem theory. Regularisation is a far-reaching strategy that can be implemented in many forms. Benning and Burger [1] give a comprehensive overview over classical and modern regularisation techniques. Often, they rely on the assumption of a certain regularity of the parameters, concerning e.g., their value or their gradient. A well-studied regularisation technique is Tikhonov regularisation, that adds a penalty function based on the norm of the parameters to the minimisation problem.

In EPMA we mainly think of regularisation as the definition of a parametrisation of the material description using $\rho(x; p)$. Instead of specifying the material as a function $\rho(x)$ with infinite dimensions, we reduce the dimensionality to a finite dimensional parameter vector p, which parametrises the mass concentrations $\rho(x; p)$. The parametrisation translates the general reconstruction problem, which searches for mass concentrations $\rho*(x)$, into the reconstruction problem, which searches for parameters $p*$ that describe structure in the material.

Reducing the variability of the unknown $\rho(x)$ into a predefined function $\rho(x; p)$ must be accompanied by the addition of carefully chosen material knowledge, because the specification of a parametrisation predefines all possible reconstruction results. Furthermore, the parametrisation should fit the available measurements. The more flexible the parametrisation is, the more measurements have to be provided, otherwise the measurements lack enough information and the reconstruction result is ambiguous.

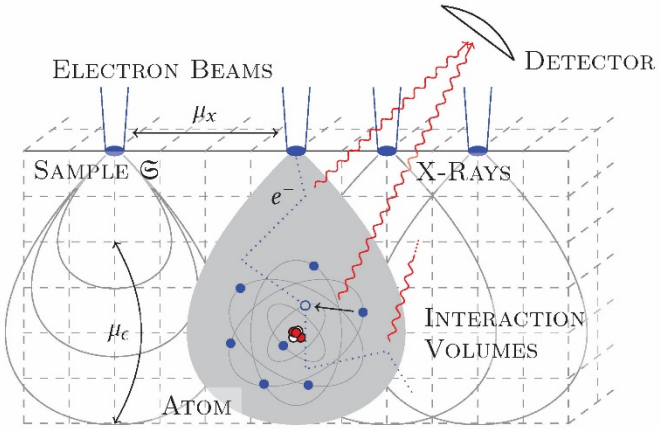

Figure 1. To increase the resolution of EPMA we use multiple experiments with electron beams at different positions μ_x and different energies μ_ϵ. Once the interaction volumes inside the sample start to overlap, a sub-scale inversion must use all experimental data to extract a spatial variation of mass concentrations.

3. *A DETERMINISTIC EPMA INVERSION FRAMEWORK*

The diversity of questions that are posed to EPMA illustrates the need to develop a reconstruction method, which remains general in the material parametrisation. We base our model on the same mathematical framework as Monte Carlo models. The electron transport is governed by the Boltzmann equation, however, instead of random sampling we rely on a deterministic approximation of the Boltzmann equation [2-5]. This allows the exact computation of gradients, the main building block of reconstruction methods. Gradients based on Monte Carlo models are polluted by statistical noise and their use in reconstruction methods is restricted.

On top of the *k*-ratio model, we propose to use a combination of algorithmic differentiation [6-7] and the adjoint state method [8] to compute gradients of the *k*-ratio model. Algorithmic differentiation is a method to compute gradients of numerical functions in a systematic (usually even automatic) and efficient manner. The adjoint state method describes a way to efficiently differentiate models based on partial differential equations (our Boltzmann approximation). The combination of both allows us to remain generic both in the objective function and the material parametrisation.

The implementation of the forward model as well as the inversion procedure is done in the programming language julia , which is a rapidly growing coding framework focussing on numerical methods and scientific computing. While providing a convenient programming syntax, it also enables high computational efficiency due to its just-in-time compiler and the concept of dynamic dispatch. It might also be the language of choice for further development of the reconstruction method, because using the concept of dynamic dispatch, various optimisations of the reconstruction method based on different parametrisations can be implemented conveniently.

4. DETERMINISTIC MODELLING

We use a deterministic *k*-ratio model pioneered in [4, 5]. The material is specified by its distributions of mass concentrations as the input to the forward problem and we discuss below the successive parts in the computation of *k*-ratios.

4.1. The intensity of generated X-rays

The intensity of generated X-rays $I_{(Z,j)}$ is a composition of multiple consecutive model parts:

$$I_{(Z,j)}(\rho) = \mathcal{A}_{(Z,j)}(\rho) \circ \mathcal{X}_{(Z,j)}(\rho) \circ \phi_{(Z,j)} \circ \Psi(\rho) \tag{2}$$

Beginning with the innermost part, they are given by the following processes. The transport of induced electrons inside the sample, quantified by the electron fluence $\Psi(\epsilon, x, \Omega) = |v(\epsilon)|n(\epsilon, x, \Omega)$, where $n(\epsilon, x, \Omega)$ is the number density of electrons with energy ϵ at position x moving in direction Ω and $v(\epsilon)$ the velocity of electrons. The ionisation distribution (x) of atoms leading to the emission of X-rays. The X-ray generation distribution $\mathcal{X}(x)$ which combines the ionisation distribution $\phi(x)$ with the actual presence of atoms, and the attenuation $\mathcal{A}$ experienced by the X-rays due to absorption and scattering.

While in Eq. (2) direct dependence of the model operators on the mass concentrations is highlighted by $\cdot(\rho)$, later we highlight the dependency of a realisation of each operator on the electron energy ϵ, the position x and the direction Ω. Note that through the parts of the model, the dimensionality of the variables decreases from $(\epsilon, x, \Omega) \in \mathbb{R}^+ \times \mathbb{R}^3 \times S^2$ to a scalar $I_{(Z,j)} \in \mathbb{R}$.

X-rays, which are generated inside the sample, are attenuated while passing through to reach the detector. The attenuation of X-rays, which are traveling along an axis (described by $z \in \mathbb{R}$) is commonly modelled using the Beer-Lambert law [9], which in the case of a constant attenuation coefficient μ simplifies to

$$\mathcal{I}(z) = \mathcal{I}_0 \exp(-\mu z) \tag{3}$$

In our model, X-rays are generated from a continuous field, hence the initial intensity is $\mathcal{I}_0 = X(x)$. The attenuation factor for a position x in the material is the line integral from x to the $\int_{d(x)} \cdot \, \mathrm{d}\bar{z}$. The detected intensity is then given by the integral over the whole material.

$$\mathcal{A}_{(Z,j)}(\mathcal{X}_{(Z,j)}) = \int_{\mathbb{R}^3} \exp\left(-\int_{d(x)} \mu_{(Z,j)}(\bar{z})\, \mathrm{d}\bar{z}\right) \mathcal{X}_{(Z,j)}(x)\, \mathrm{d}x \tag{4}$$

The linear attenuation coefficient $\mu_{(Z,j)}(x)$ for compounds can be modelled by linear combination with mass concentrations ρ_i in the form $\mu_{(Z,j)}(x) = \sum_{i=1}^{n_e} \rho_i(x) \left(\frac{\mu}{\rho}\right)_{i,(Z,j)}$ whereby the mass attenuation coefficients $\left(\frac{\mu}{\rho}\right)_{i,(Z,j)}$ for elements i are interpolated for the characteristic energy of an X-ray (Z,j). Implementations and data for mass absorption coefficients can be found in [10-12].

To compute the X-ray generation distribution for an X-ray (Z,j), we weigh the ionisation distribution $\phi_{(Z,j)}(x)$ by the number of atoms of element Z per unit volume ρ_Z/A_Z and the fluorescence yield $\omega_{(Z,j)}$ for the transition (Z,j).

$$\mathcal{X}_{(Z,j)}(\phi_{(Z,j)}) = \frac{\rho_Z(x)}{A_Z} \omega_{(Z,j)} \phi_{(Z,j)}(x) \tag{5}$$

Thereby (x) is the mass concentration and A_Z the atomic mass of element Z.

The ionisation distribution field $\phi_{(Z,j)}(x)$ of X-ray (Z,j) is given by product of the number density of electrons $n(\epsilon, x, \Omega)$ traveling with velocity $v(\epsilon)$ in direction Ω and the ionisation cross-section $\sigma_{(Z,j)}(\epsilon)$ describing the fraction of collisions leading to core shell ionisations, which may result in the emission of (Z,j) X-rays.

$$\phi_{(Z,j)}(x) = \int_0^\infty \sigma_{(Z,j)}(\epsilon) \int_{S^2} \underbrace{|v(\epsilon)| n(\epsilon, x, \Omega)}_{=:\Psi(\epsilon,x,\Omega)} \mathrm{d}\Omega\, \mathrm{d}\epsilon \tag{6}$$

Implementations and data for ionisation cross-sections and fluorescence yields can be found in [11, 13-16].

Due to the high dimensionality ($\mathbb{R}^+ \times \mathbb{R}^3 \times S^2$) of the electron number density $n(\epsilon, x, \Omega)$ and the electron fluence $\Psi(\epsilon, x, \Omega)$, a simulation of either is complex. Hence, it is advantageous to derive a model for the averaged electron fluence. In Eq. (6), the electron number density only appears weighted by the magnitude of velocity $|v(\epsilon)|$ and averaged in direction $\Omega \in S^2$. We define

$$\psi_0^0(\epsilon, x) = \int_{S^2} |v(\epsilon)| n(\epsilon, x, \Omega) \, \mathrm{d}\Omega \tag{7}$$

and describe the P_N-model, a moment expansion that governs ψ_0^0 (the zeroth moment of the electron fluence Ψ), in the next section.

4.2. The electron fluence: The P_N-moment-model

For a detailed derivation of the P_N-model see [17, 18]. Here only the expansion using the method of moments [12] is described.

The linear Boltzmann equation [19] describes particle transport, where the self-interaction between particles can be neglected and only (elastic and inelastic) scattering with the background medium is considered. In the context of EPMA, the time dependence in the linear Boltzmann equation is negligible and the inelastic scattering operator is replaced by its continuous slowing down approximation (CSD). The continuous energy loss is modelled using the stopping power $S(\epsilon, x)$, the average energy loss per path length. The stopping power governs parts of the scattering operator in the linear Boltzmann equation, the leftover parts we call $Q(\epsilon, x)[\Psi]$. The resulting transport equation is an evolution equation for the electron fluence Ψ $\epsilon, x, \Omega = |(\epsilon)| n(\epsilon, x, \Omega)$ given by:

$$-\partial_\epsilon (S(\epsilon, x)\Psi(\epsilon, x, \Omega)) + \Omega \nabla_x \Psi(\epsilon, x, \Omega) = Q(\epsilon, x)[\Psi(\epsilon, x, \Omega)] \tag{8}$$

4.3. Spectral Galerkin approximation

As mentioned, it is expensive to solve Eq. (8) numerically, hence we will reduce the model complexity using a Galerkin method, which expands $\Psi(\epsilon, x, \Omega)$ into a linear combination of moments and basis function in Ω. The expansion is called the method of moments [12]. The spherical harmonics [20], an orthonormal set of functions $S^2 \to \mathrm{R}$, have proven to be suitable basis functions, because they possess favourable properties, which are inherited to the resulting model (the P_N-model). The real spherical harmonic $Y_l^k : S^2 \to \mathbb{R}$ degree $l \in \mathbb{N}_0$ and of order k ($|k| \leq l$) maps a direction $\Omega(\mu, \varphi) \in S^2$, also represented by polar $\mu \in [0, \pi]$ and azimuthal (longitudinal) angle $\varphi \in [0, 2\pi]$, to the real numbers R.

We apply the method of moments to the BCSD as given in Eq. (8). The electron fluence Ψ is approximated by a linear combination of spherical harmonics up to degree $l \leq N \in \mathbb{N}^0$

$$\Psi(\epsilon, x, \Omega) \approx \Psi_{P_N}(\epsilon, x, \Omega) = \sum_{l \leq N, |k| \leq l} \psi_l^k(\epsilon, x) Y_l^k(\Omega) \tag{9}$$

The coefficients $\psi_l^k(\epsilon, x)$ are the moments of the electron fluence Ψ and, since spherical harmonics form an orthonormal basis of S^2, the moment ψ_l^k is given by the scalar product

$$\psi_l^k(\epsilon, x) = \int_{S^2} \Psi(\epsilon, x, \Omega) Y_l^k(\Omega)\, \mathrm{d}\Omega \tag{10}$$

Moments ψ_l^k of higher degree $l > N$ are assumed to be $\ll 1$, therefore, negligible. The zeroth spherical harmonic $Y_l^k : S^2 \to \mathbb{R}$ is constant, so we can identify $\psi_0^0(\epsilon, x)$ with the variable in Eq. (6).

From Eq. (8) evolution equations for the moments ψ_l^k are derived by testing (multiplying and integrating: $\int_{S^2} \cdot Y_{l'}^{k'}(\Omega)\, \mathrm{d}\Omega$) with spherical harmonics. Testing with the set of same spherical harmonics ($l' \leq N$, $|k'| \leq l'$), which are used in the approximation Ψ_{P_N} leads to a system of equations, the P_N-model

$$-\partial_\epsilon(S\psi) + A^{(x)}\partial_x\psi + A^{(y)}\partial_y\psi + A^{(z)}\partial_z\psi + C\psi = 0 \tag{11}$$

The unknown variables are the coefficients $\psi = \{\psi_l^k\}_{l \in \mathbb{N}_0, |k| \leq l}$ used in the P_N approximation, the moments of the electron fluence Ψ. We derive the summands in Eq. (11) from Eq. (8) individually.

4.3.1. Stopping power. The first term in Eq. (8) is linear in Ψ and the spherical harmonics form an orthonormal basis, hence the term diagonalises in the moment method. The stopping power S is a material property, where for a compound we derive additivity using the mass concentrations $\rho(x)$ from the additivity approximation for cross-sections [21]

$$S(\epsilon, x) = \sum_{i=1}^{n_e} \rho_i(x) S_i(\epsilon) \tag{12}$$

Thereby $S_i(\epsilon)$ is a specific stopping power of pure element i. For the stopping power of pure elements there exists multiple models, e.g., a model based on the Bethe-Loss formula [22] or interpolation tables from a more advanced model [5, 16]; we use the latter in our current implementation.

4.3.2. Transport coefficient. The transport coefficient C is derived from the scattering operator $Q(\epsilon, x)[\Psi]$ that models elastic and deflections of inelastic collisions (the energy loss is modelled by the stopping power). The scattering operator Q is linear in the electron fluence Ψ, so if we replace Ψ with its P_N approximation and test with the spherical harmonic $Y_{l'}^{k'}$, we derive the transport coefficient matrix C by similar argument as for the stopping power.

$$C_{(l,k),(l',k')} = -\int_{S^2} Q(\epsilon, x)[Y_l^k] Y_{l'}^{k'}\, \mathrm{d}\Omega = -\int_{\mathbb{S}^2} C_l Y_l^k Y_{l'}^{k'}\, \mathrm{d}\Omega = -C_l \delta_{(l,k),(l',k')} \tag{13}$$

Spherical harmonics are eigenfunctions of isotropic operators, hence C is diagonal with entries C_l, which are the eigenvalues of the scattering operator Q corresponding only to the degree l of the spherical harmonic ψ_l^k. As for the stopping power, we derive additivity for the transport coefficients using the mass concentrations $\rho_i(x)$ from the additivity approximation [26]

$$C_l(\epsilon, x) = \sum_{i=1}^{n_e} \rho_i(x) C_{l,i}(\epsilon) \tag{14}$$

The specific coefficients $C_{l,i}(\epsilon)$ for the pure elements are derived from scattering cross-sections generated using the code from [24], which in [5] are tabulated for the different degrees of the spherical harmonics.

4.3.3. Advection matrices. By testing the advection operator $\Omega \cdot \nabla_x \Psi$ with the spherical harmonic $Y_{l'}^{k'}$ the advection matrices $^{(x)}$, $A^{(y)}$ and $A^{(z)}$ are identified using the recursion relation given for spherical harmonics. Note that the advection matrices are very sparse and possess a specific pattern with respect to the classification of the spherical harmonics. Furthermore, all advection matrices are symmetric $^{(n)T} = A^{(n)}$. The sparsity of the advection matrices is exploited in the numerical method and paves the way towards an efficient implementation of the P_N-model.

4.3.4. N-boundary conditions. Initial conditions for the electron fluence Ψ in energy are specified at a given maximum energy ϵ_{init}.

$$\Psi(\epsilon_{\text{init}}, x, \Omega) = \Psi_0(x, \Omega) \tag{15}$$

The translation of an initial condition in energy $\Psi_0(x,\Omega)$ into its moments $\psi_{l,0}^k(x)$ straightforward. Using Eq. (10), the initial condition Ψ_0 is expanded into the respective moments. In the following experiments, we will typically use $\Psi_0(x,\Omega) = 0$, assuming that no beam electrons are present inside the sample at $\epsilon = \epsilon_{\text{init}}$.

For an implementation, the spatial variable x is confided to $\mathfrak{S} \subset \mathbb{R}^3$. Then a proper treatment of boundary conditions in space is necessary. At a point $x \in \partial\mathfrak{S}$ with n the outward boundary normal, we are allowed to prescribe the ingoing part of the electron fluence Ψ

$$\Psi(\epsilon, x, \Omega) = \Psi_{\text{in}}(\epsilon, x, \Omega) \quad \Omega \cdot n < 0 \tag{16}$$

The boundary conditions for the moments ψ are given by Galerkin projections of (16) with spherical harmonics which are odd functions with respect to the normal direction on S^2. See [17] for more details.

4.3.5. Beam parameters. The electron beam hits the sample at a surface (in our examples usually $\{(x_1, x_2, x_3) \in \mathfrak{S} | x_1 = 0\}$). We model the beam using an isotropic Gaussian distribution on the material surface, a Gaussian distribution in energy and a three-dimensional

Von-Mises-Fisher distribution (a distribution defined on S^2) in direction. Using respective means μ_x and μ_ϵ, variances σ_x and σ_ϵ as well as the mean direction μ_Ω and concentration parameter κ of the Von-Mises-Fisher distribution, we define

$$\Psi_{\text{in}}(\epsilon, x, \Omega) = \mathcal{N}\left((x_2, x_3)^T | \mu_x, \text{diag}(\sigma_x)\right) \mathcal{N}(\epsilon | \mu_\epsilon, \sigma_\epsilon) \mathcal{F}(\Omega | \mu_\Omega, \kappa) \tag{17}$$

where $\mathcal{N}$ is the probability density function of the Gaussian distribution and $\mathcal{F}$ is the probability density function of the Von-Mises-Fisher distribution. Integration of $\mathcal{F}$ into the respective moments $\int_{n\cdot\Omega<0} \Psi_{\text{in}} Y_l^k(\Omega)\, \mathrm{d}\Omega$ is performed numerically.

5. *NUMERICAL IMPLEMENTATION*

Computing *k*-ratios using the model presented above is based on StaRMAP, a numerical method for the solution of the moment expansion for the electron fluence, based on a generic moment equation and detail on the solution of the P_N-equation. The main characteristic of StaRMAP is the discretisation of the solution variable on staggered grids. Allowed by a specific structure of the equation, the staggered grid discretisation leads to an efficient second order approximation. It is originally published in [25] and already used in the context of electron transport in EPMA in [5, 7, 19].

6. *MATERIAL REPRESENTATION*

The particular choice of a model of mass concentrations ρ is problem dependent and should be conducted with great care and a particular material in mind.

In this section, we provide models for mass concentrations which are utilised to conduct the reconstruction experiments presented in this paper. Thereby we distinguish between mass concentration models and parametrisations. The former is the relation of mass concentrations with other physical quantities, which will be discussed more in the presentation, and the latter is the mathematical parametrisation of a function in 3D for which we give more details below. Combining a mass concentration model with a parametrisation yields the relation

$$\rho(x; p) : \mathbb{R}^3 \times \mathbb{R}^{n_p} \to \mathbb{R}^{n_e} \tag{18}$$

that is, a parametrisation of the function $\rho(x)$ which returns mass concentrations of n_e elements given a position x inside the material and n_p parameters, which describe the material.

7. PARAMETRISATION MODELS

In this section, we propose some parametrisations for the discretisation of a multivariate 3D function. Although we visualise the concepts only in 2D, the extension to 3D or the reduction to 1D is straightforward. We denote the parametrised function with $P(x; p) : \mathbb{R}^3 \times \mathbb{R}^{n_p} \rightarrow \mathbb{R}^{n_o}$ its parameters with $p \in \mathbb{R}^{n_p}$. We denote the number of output values of the parametrisation P with n_o. For the sake of comparability, we precisely formulate the number of required parameters n_p for each parametrisation.

7.1. Piecewise-constant parametrisation

Assume that the reconstruction domain is split into several cuboids(3D) / rectangles(2D), see Fig. 2a, with aligned interfaces in all dimensions. We specify a rectangular box by

$$\mathcal{B}_{i,j,k} = \{(x, y, z) \in \mathbb{R}^3 | x_i < x \leq x_{i+1}, y_j < y \leq y_{j+1}, z_k < z \leq z_{k+1}\} \tag{19}$$

where the interfaces are given by $\{x_i\}_{i=1,\ldots,n_x}$, $\{y_j\}_{j=1,\ldots,n_y}$ and $\{z_k\}_{k=1,\ldots,n_z}$ with n_x, n_y and n_z the number of interfaces in each dimension. Based on the subsets, we define the 3D piecewise-constant parametrisation by

$$P(x; p) = \begin{cases} p_{i,j,k} & x \in \mathcal{B}_{i,j,k} \\ p_{\text{out}} & \text{else} \end{cases} \tag{20}$$

In each of the boxes $B_{i,j,k}$ the parametrisation P is constant with a value defined by the parameters $p_{i,,k}$. If x happens to lie outside all the boxes, we assign p_{out}. The number of parameters is given by $n_p = ((n_x - 1)(n_y - 1)(n_z - 1) + 1)n_o$. Because $p$out counts as an additional "box", we add 1. Note that the positions of the interfaces x_i, y_j and z_k are fixed and not part of the parameters.

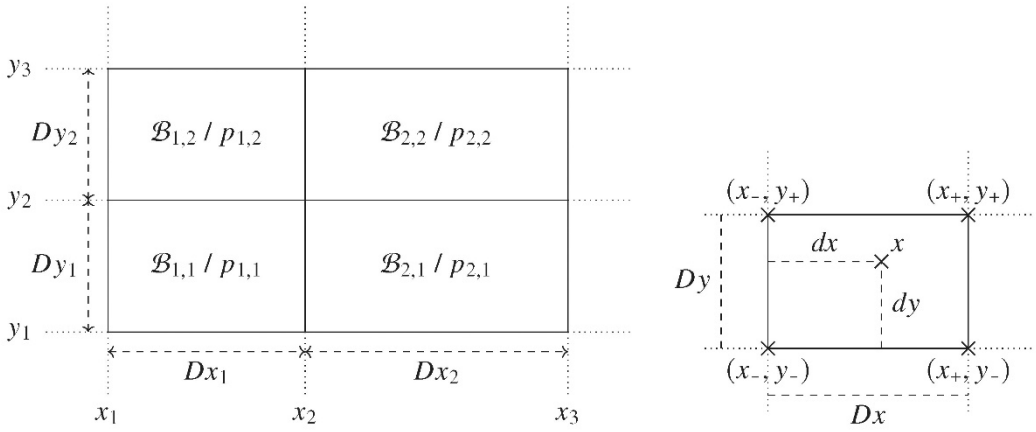

Figure. 2. a) Interfaces of the boxes $B_{i,j}$ are defined by x_i and y_j. The boxes are not required to be equally sized and their side lengths are defined by Dx_i and Dy_i. Inside each box $B_{i,}$ the function value is constant ($x \in \mathrm{B}_{i,}$) = $p_{i,j}$. b) Shows a box with vertices (x_-, y_-), (x_+, y_-), (x_+, y_+) and (x_-, y_+). Distances of x from the interfaces are denoted with dx resp. dy and the side lengths of the box with Dx and Dy.

7.2. Linear parametrisation

The linear parametrisation is also based in the splitting of the reconstruction domain into several boxes, see Fig. 2b. But instead of specifying the value of P inside each box, we specify the value of P on the vertices of the boxes. We define the linear interpolation by

$$P(x, p) = \begin{cases} \mathcal{I}(x; p_{i,j,k}, p_{i+1,j,j}, p_{i,j+1,k}, \ldots, p_{i+1,j+1,k+1}) & x \in \mathcal{B}_{i,j,k} \\ \mathcal{I}(x; p_{\text{out}}) & else \end{cases} \tag{21}$$

where I denotes 3D linear interpolation of the values on the vertices.

We visualise the linear interpolation in 2D in Fig. 2b and derive the interpolation formula. Given a point (x, y) which is inside the Rectangle $\{(x, y)|x_- \le x < x_+, y_- \le y < y_+\}$, we derive interpolation weights η_x and η_y

$$\eta_x = \frac{dx}{Dx} = \frac{x - x_-}{x_+ - x_-} \quad \eta_y = \frac{dy}{Dy} = \frac{y - y_-}{y_+ - y_-} \tag{22}$$

Based on the parameters defined on the vertices p_{--}, p_{+-}, p_{-+} and p_{++} the interpolation is given by

$$\mathcal{I}(x; p_{--}, p_{+-}, p_{-+}, p_{++}) = (1 - \eta_x)(1 - \eta_y)p_{--} + \eta_x(1 - \eta_y)p_{+-} + (1 - \eta_x)\eta_y p_{-+} + \eta_x\eta_y p_{++} \tag{23}$$

A linear interpolation using n_x, n_y and n_z interfaces has $n_p = (n_x n_y n_z + 1)_0$ parameters. We add 1 if we additionally specify a value for points outside all interfaces.

8. RECONSTRUCTION AS AN OPTIMISATION PROBLEM

The formulation of the reconstruction as an optimisation problem mainly consists of the following steps: The definition of the parameters p which are searched for, the definition of the forward model (p) and the definition of the objective

$$\text{disc}(k(p), k^{\text{exp}}) \tag{24}$$

as some measure of discrepancy between modelled $k(p)$ and measured k^{exp} k-ratios. The reconstruction result is then the set of parameters p^* for which the modelled k-ratios have the smallest discrepancy from the measured k-ratios.

$$p^* = \arg\min_p \text{disc}(k(p), k^{\text{exp}}) \tag{25}$$

Usually the discrepancy $\text{disc}(\cdot,\cdot)$ denotes a norm, therefore $\text{disc}(\cdot,\cdot) \ge 0$. However, we cannot expect to find p^* such that $\text{disc}(k(p^*), k^{\text{exp}}) = 0$ in a real reconstruction problem, because of imperfect modelling and the presence of noise.

Classical reconstruction approaches, e.g., matrix correction methods for homogeneous materials or layered specimen based on (ρz)-curves, define homogeneous mass concentrations or the mass thickness of layers as the parameters p. The k-ratio model either bases on multiplicative correction factors or the integration of (ρz)-curves. The discrepancy $\mathrm{disc}(\cdot,\cdot)$ is defined as the squared error of modelled and measured k-ratios

$$\mathrm{disc}(k(p), k^{\mathrm{exp}}) = \sum_{(Z,j)} (k_{(Z,j)}(p) - k^{\mathrm{exp}}_{(Z,j)})^2 \tag{26}$$

The use of the squared error as the objective function is not limited to matrix correction methods and can be used analogously with our model.

8.1. Statistical interpretation

Defining the squared error as the objective function is very common, but may feel arbitrary. Inverse problem theory justifies the choice of the squared error function by deriving it from statistical assumptions [26]. The assumptions simultaneously allow a statistical interpretation of the reconstruction result p^*.

Inverse problem theory [26, 27] relies on the assumption, that the observation (the k-ratio measurements k^{exp}) relate with the model parameters p through

$$k^{\mathrm{exp}} = k(p) + \eta \tag{27}$$

where η is a random variable. More generally, one defines the likelihood, the probability that based on the parameters p the model (p) produces the data k^{exp}. The probability density function (pdf) of the likelihood is

$$\pi(k^{\mathrm{exp}}|p) = \pi_\eta(k^{\mathrm{exp}} - k(p)) \tag{28}$$

where π_η is the pdf of the random variable η, which is usually referred to as noise, but might also include model uncertainties.

Additionally, the prior knowledge about the material is encoded in the prior pdf (p). Using Bayes Theorem, the resulting uncertainty about the material is the posterior pdf

$$\pi(p|k^{\mathrm{exp}}) = \frac{\pi(k^{\mathrm{exp}}|p)\pi(p)}{\int \pi(k^{\mathrm{exp}}|p)\pi(p)\,\mathrm{d}p} \tag{29}$$

The posterior is the probability, that p represents the reality given the measured observation k^{exp}. The posterior $(p|k^{\mathrm{exp}})$ combines likelihood $\pi(k^{\mathrm{exp}}|p)$ and prior $\pi(p)$ and defines the solution of the inverse problem. The statistical approach to inverse problems is philosophical and for problems of a certain size not (yet) applicable. However, it motivates concepts that are applied to solve real world reconstruction problems.

The maximum likelihood estimate p^* for EPMA is

$$p^* = \arg\max_p \pi(k^{\exp}|p) \tag{30}$$

the maximum of the probability density function of the likelihood Eq. (28). Analogously we can write

$$p^* = \arg\min_p \underbrace{-\pi(k^{\exp}|p)}_{=\mathrm{disc}(k(p),k^{\exp})} \tag{31}$$

and define a discrepancy function. The maximum posterior estimate can be found similarly by defining

$$\mathrm{disc}(k(p), k^{\exp}) = -\pi(p|k^{\exp}) \propto -\pi(k^{\exp}|p)\pi(p) \tag{32}$$

where $\pi(p|k^{\exp})$ is the pdf of the posterior, which is proportional to the product of the likelihood pdf and the prior pdf $\pi(p)$.

In the special case of a Gaussian likelihood and a Gaussian prior, the problem to find the maximum posterior can be written as

$$p^* = \arg\min_p ||k(p) - k^{\exp}||^2_{\Sigma_L^{-1}} + ||p - \mu_p||^2_{\Sigma_P^{-1}} \tag{33}$$

where Σ_L and Σ_P are the covariance matrices of likelihood and prior and μ_P the mean of the prior. With $||x||^2_A = x^T Ax$ we denote weighted least squares. The special case of the maximum posterior approximation with Gaussian probabilities is also known as Tikhonov regularisation, a well studied regularisation technique [1]. When neglecting the regularisation term $||p - \mu_p||^2_{\Sigma_P^{-1}}$ and choosing an isotropic covariance $\Sigma_L = \sigma_L^2 I$, Eq. (33) is equivalent to minimising the squared error Eq. (26).

A justification of the Gaussian assumptions or the definition of a proper likelihood and prior is beyond the scope of this work, because it requires a detailed uncertainty quantification of modelling errors and measurement noise. Furthermore, it is unclear if a general definition of the objective function for reconstruction in EPMA is possible, because the inverse problem is so multifaceted. In this abstract, we employ the squared error as the discrepancy function.

9. SHOWCASE: 1D RECONSTRUCTION OF INTERFACES

In the talk, we will give a number of showcases to study the performance of the approach. Here, we present the reconstruction of a coated material consisting of iron and nickel with a sharp (discontinuous) and a diffusive (continuous) interface between the layers. By means of this

example we will compare the piecewise linear and piecewise constant parametrisations described above. For a fair comparison, the number of parameters in each parametrisation is chosen to be 10. For the piecewise-constant parametrisation, the interval [0 nm, −300 nm] is divided in depth into 10 equal parts. Note that the location of the sharp interface aligns with one of the interfaces of the piecewise-constant parametrisation. For the linear interpolation, we discretise the interval in 9 equal parts. We strongly enforce the constraint for the volume fractions $\varphi_{Ni} = 1 - \varphi_{Fe}$, hence at every location a scalar $P(x; p)$ completely describes the material. To resolve the interface position and structure, we compare k-ratios from multiple different beam energies between 9 keV and 15 keV. Secondary fluorescence effects are neglected. Additional P_N-model settings and the considered X-rays are tabulated in Table 1. We use the squared error of k-ratios as the objective function and choose the BFGS method implemented in OPTIM.JL [28] as optimisation method.

Table 1. Model settings used for the reconstruction of the 1D interfaces.

domain $\mathfrak{S}$	$(-500\text{nm}, 0\text{nm})$ $n_x = 100$
energies $[\epsilon_{\text{cut}}, \epsilon_{\text{min}}]$	(7.0keV, 15.5keV)
approximation order P_N	$N = 9$
beam $\epsilon, \sigma_\epsilon$	$\{9, 10.5, 12, 13.5, 15\}$keV, 0.1keV
elements/x-rays	$(Ni, K-L_2)$, $(Ni, K-L_3)$, $(Fe, K-L_2)$ and $(Fe, K-L_3)$

In Fig. 3, the reconstructed density of the material with a sharp interface is visualised using the different parametrisations. From initial configurations (piecewise-constant and linear: 0.5 Fe and 0.5 Ni) the parametrisations iterate towards the reference density (black line) during the optimisation. We visualise the initial, 1st, 5th and 100th iteration. The inability of the linear parametrisation to represent discontinuities becomes apparent. However, the piecewise-constant parameterisation only approximates perfectly because the interface matches the interface of the reference.

In Fig. 4, the reconstructed density of the material with a diffusive interface is visualised. Except for the reference material, exactly the same settings as for the reconstruction of the sharp interface are used. Again, the parametrisations iterate towards the reference density (black line). For the diffusive interface, none of the parametrisations can reconstruct the interface perfectly, but the linear performs better than the piecewise-constant parametrisation.

In Fig. 5, we visualise the normalised error, the value of the objective function $||k(p) - k^{\text{exp}}||^2$, the error in the mass concentrations $||\rho(x) - \rho^{\text{true}}||^2$ and the error of additional k-ratio measurements $||k_+(p) - k_+^{\text{exp}}||^2$ (with beam energies 11 keV and 14 keV) during the optimisation iterations. The kinks in the error of the objective function are an artefact of the OPTIM.JL implementation. Their default implementation bases on the combination of a line search method [29] and the BFGS algorithm presented in [30].

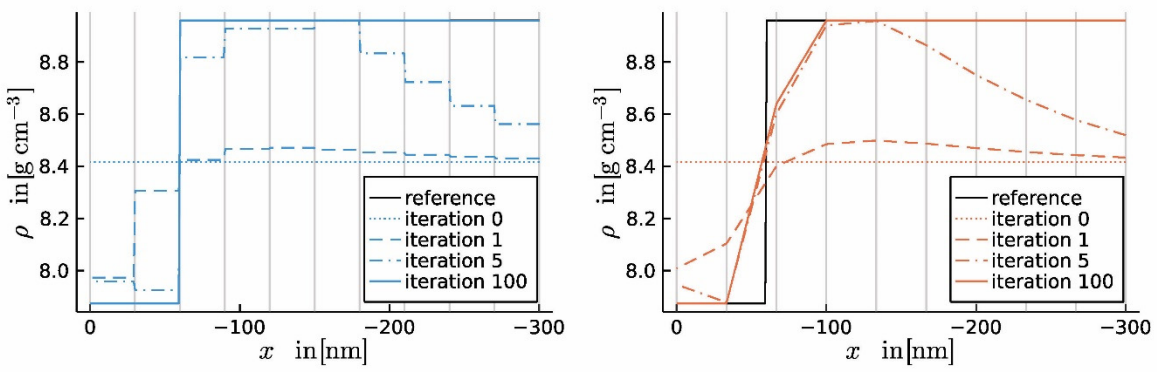

(a) Piecewise-Constant **(b)** Linear

Figure 3. The reconstructed density of a material with a sharp interface between an iron layer covering a nickel substrate. We use the material parametrisations based on piecewise linear and piecewise constant functions for the reconstruction. The geometry (interfaces) are visualised by grey vertical lines. The black line shows the reference density. All parametrisations converge. The piecewise-constant parametrisation has a clear advantage, because the interface aligns with an interface of the parametrisation. The linear parametrisation cannot approximate the discontinuous interface, hence it converges to the presented smoothed representation.

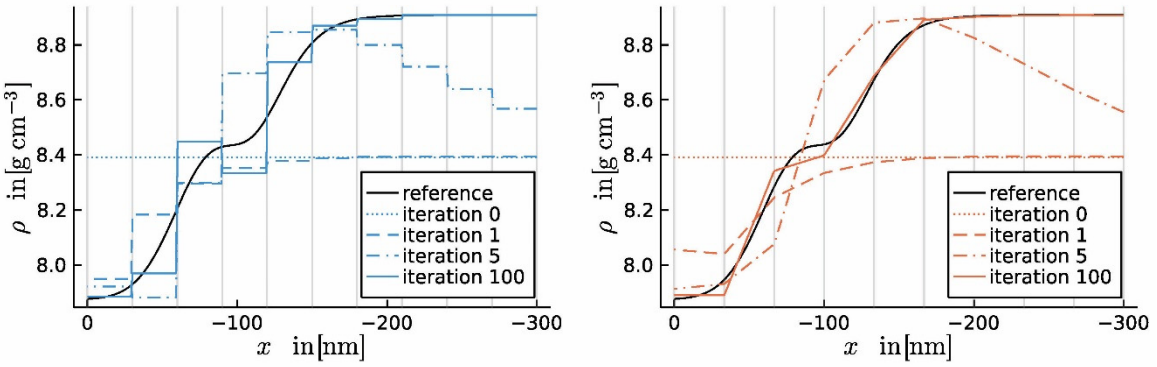

(a) Piecewise-Constant **(b)** Linear

Figure 4. The reconstructed density of a material with a diffusive interface between an iron layer covering a nickel substrate. We again use linear and piecewise constant functions for the material parametrisations. The geometry (interfaces) are visualised by grey vertical lines. The black line shows the reference density. All parametrisations converge. None of the parametrisations can represent the interface perfectly. The bilinear performs better for this example, because of its flexibility to approximate continuous functions.

Differences in the performance of the different parametrisations are clearly visible. The material error for the piecewise-constant parametrisation for the sharp interface is by far the smallest, due to the possible perfect reconstruction. Comparing the material error for piecewise-constant and linear parametrisation for the sharp and the diffusive interface, they vary.

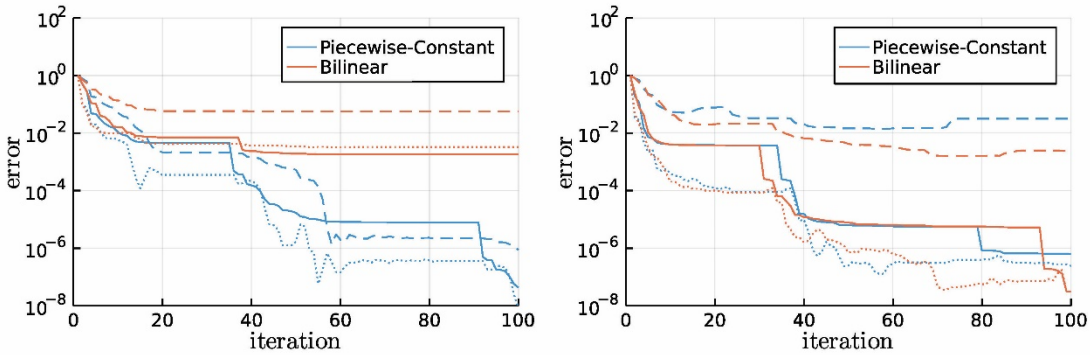

(**a**) Sharp Interface (**b**) Diffusive Interface

Figure 5. The value of the objective function and additional reconstruction quality measures during the iterations of the optimisation for all parametrisations. The objective function $\|(p) - k^{\text{exp}}\|^2$ is visualised as a solid line. Also, the material error $\|(x) - \rho^{\text{true}}\|^2$ (dashed line) and the error of k-ratios $||k_+(p) - k_+^{\text{exp}}||^2$ (dotted line) from additional beam energies (11 keV and 14 keV) is plotted.

A correlation between the material error and the error of additional k-ratios would be beneficial, but is hard to obtain. Ideally, both would behave similarly, because then we could propose the error in additional k-ratios as a suitable reconstruction quality measure.

10. ACKNOWLEDGEMENTS

The co-authors Gaurav Achuda and Tamme Claus are funded by the German Research Foundation (DFG) through the individual research grant with project number DFG-466010736.

11. REFERENCES

[1] Benning M and Burger M 2018 *Modern regularization methods for inverse problems*. arXiv:1801.09922
[2] Larsen E W, Miften M M, Fraass B A and Bruinvis I A 1997 *Med. Phys.* **24** 111-125
[3] Duclous R, Dubroca B and Frank M 2010 *Phys. Med. Biol.* **55** 3843-3857
[4] Mevenkamp N 2016 *Inverse modeling in electron probe microanalysis based on deterministic transport equations*. MSc thesis. [Aachen, Germany: RWTH Aachen]
[5] Bünger J 2021 *Three-dimensional modelling of x-ray emission in electron probe microanalysis based on deterministic transport equations*. PhD thesis. [Aachen, Germany: RWTH Aachen University] No.: RWTH-2021-05180
[6] Naumann U 2011 *The art of differentiating computer programs. Software, environments and tools*. [Philadelphia, PA: Society for Industrial and Applied Mathematics]

[7] Griewank A 2003 *Acta Numerica* **12** 321-398
[8] Plessix R-E 2006 *Geophys. J. Int.* **167** 495-503
[9] Pinard P T 2016 *Electron probe microanalysis of carbon containing steels at a high spatial resolution*. PhD thesis. [Aachen, Germany: RWTH Aachen University]
[10] Ritchie N 2021 FFAST.jl. github.com/usnistgov/FFAST.jl
[11] Ritchie N 2021 NeXLCore.jl. github.com/usnistgov/NeXLCore.jl
[12] Chantler C T, Olsen K, Dragoset R A, Chang J, Kishore A R, Kotochigova S A and Zucker D S 2009 *X-ray form factor, attenuation, and scattering tables*. NIST Standard Reference Database 66
[13] Ritchie N 2020 BoteSalvatICX.jl. github.com/usnistgov/BoteSalvatICX.jl
[14] Bote D, Salvat F, Jablonski A and Powell C J 2009 *Atom. Data Nucl. Data Tables* **95** 871-909
[15] Bote D and Salvat F 2008 *Phys. Rev. A* **77** 042701
[16] Cullen D E, Hubbell J H and Kissel L 1997 *EPDL97: the evaluated photo data library '97 version*. Technical Report UCRL-50400-Vol.6-Rev.5. [Livermore, Ca: Lawrence Livermore National Lab.]
[17] Bünger J, Sarna N and Torrilhon M 2021 Stable boundary conditions and discretization for PN equations. arXiv:2004.02497
[18] Buenger J, Richter S and Torrilhon M 2022 *Microsc. Microanal.* **28** 454-468
[19] Cercignani C 1988 *The Boltzmann equation and its applications*. in: Applied Mathematical Sciences, vol. 67. [New York, NY: Springer-Verlag]
[20] Müller C 1966 *Spherical harmonics*. in: Lecture notes in mathematics, vol. 17. [Berlin-Heidelberg, Germany: Springer-Verlag]
[21] Salvat F, Berger M J, Jablonski A, Bronic I K, Mitroy J, Powell C J and Sanche L 2007 *Elastic scattering of electrons and positrons*. ICRU Report 77. [Bethesda, MD: International Commission on Radiation Units & Measurements]
[22] Reimer L 1998 *Scanning electron microscopy: Physics of image formation and microanalysis; 2nd edition*. [Berlin-Heidelberg, Germany: Springer-Verlag]
[23] Salvat F, Berger M J, Jablonski A, Bronic I K, Mitroy J, Powell C J and Sanche L 2007 *Elastic scattering of electrons and positrons, vol. 7*. ICRU report. [Bethesda, MD: International Commission on Radiation Units & Measurements 11 16-21
[24] Salvat F, Jablonski A and Powell C J 2005 *Computer Phys. Comm.* **165** 157-190
[25] Seibold B and Frank M 2014 StaRMAP - A second order staggered grid method for spherical harmonics moment equations of radiative transfer. arXiv:1211.2205
[26] Tarantola A 2005 Inverse problem theory and methods for model parameter estimation. in: Other titles in applied mathematics. [Philadelphia, PA: Society for Industrial and Applied Mathematics]
[27] Stuart A M 2010 *Acta Numerica* **19** 451-559
[28] Mogensen P K and Riseth A N 2018 *J. Open Source Software* **3** 615
[29] Hager W W and Zhang H 2005 *SIAM J. Optimization* **16** 170-192
[30] Nocedal J and Wright S 2006 *Numerical optimization; 2nd edition*. in: Springer Series in Operations Research and Financial Engineering. [New York, NY: Springer-Verlag]